

About the Acquisition and Processing of Ray Deflection Histograms for Transparent Object Inspection

Johannes Meyer¹, Thomas Längle², Jürgen Beyerer^{2,1}

¹ *Karlsruhe Institute of Technology KIT*

² *Fraunhofer-Institute of Optronics, System Technologies and Image Exploitation IOSB*

Abstract

Objects made from transparent materials are of great importance in our every-day life. In order to work as intended, these objects have to meet high quality criteria. Since their transparency makes many existing machine vision methods for opaque objects inapplicable, novel approaches have to be found. This paper proposes an optical inspection system based on a $4f$ light field camera in concert with parallel illumination, so that local histograms of the deflections of light rays exiting the test object can be acquired. Furthermore, the article presents two different approaches for processing these histograms of ray deflections (HORDs) in order to visualize scattering defects present in the test object. To evaluate the suitability of the proposed acquisition setup and the light field processing methods for the visualization of scattering material defects, different experiments are performed using a physically based rendering framework.

Keywords: machine vision, transparent object inspection, light field processing, image processing, histogram comparison

1 Introduction

Transparent objects and materials are of great importance. They are used in diverse kinds of industries to produce products that have to meet high quality requirements. For example, windshields of automobiles or aircrafts have to be clear, have to protect the passengers from the environmental influences, have to be mechanically durable and must not impair the driver's or pilot's sight. A further example are transparent plastic lenses used in eye-surgery, that have to precisely guide high-power laser beams as intended by the manufacturer in order to help and not harm the patient. Therefore, the respective transparent parts have to be free from material defects like absorbing or scattering particles. There exist elaborated machine vision methods for finding absorbing defects in transparent objects [Meyer, 2014]. However, the detection of scattering impurities in transparent materials with a more complex 3D-geometry is still an open research question. Since scattering defects, e.g., air bubbles, result in a deflection of the incident light rays, the directions of the light rays exiting the test object have to be captured in order to gain information about the defect. However, as both the transparent object's 3D-shape and scattering impurities can deflect light, a potential visual inspection system has to capture spatially resolved information on the direction of light rays exiting the test object. This paper shows, that an appropriately recorded light field contains the necessary information for visualizing scattering defects in transparent objects with a complex 3D-geometry, e.g., a double-convex lens. Furthermore, the present work introduces an optical setup capable of capturing such a light field and presents a mathematical framework for performing the necessary image processing steps on the acquired data.

The paper is organized as follows: Section 2 outlines work on light field processing performed by other researchers. In Sec. 3, a novel optical setup is proposed that acquires light field data suitable for transparent object inspection. Section 4 introduces a mathematical framework that paves the way for conveniently processing the light field data. Furthermore, Sec. 5 describes how scattering material defects are manifested in the light

field and how they can be extracted. The experiments carried out in order to evaluate the presented approach are presented and discussed in Sec. 6. Finally, Sec. 7 provides a summary of all the findings and closes the paper with a short outlook.

2 Related work

The idea of light field cameras is not new. They first were described by Gabriel Lippmann in the early 20th century [Lippmann, 1908]. In the recent years, the technology behind light field cameras emerged greatly, especially because of the research performed by Ng et al. [Ng et al., 2005] and Perwass and Wietzke [Perwass and Wietzke, 2012]. However, the performed research has mainly been targeted on the consumer photography market and not on machine vision applications. This is why there are only a few research groups working on visual inspection applications using light field processing. One of them—the group of [Štolc et al., 2014]—employed multiple line scan cameras to capture the light field reflected by test objects lying on a conveyor belt. Therefore, the cameras were all tilted by a certain angle so that they observed a common line on the conveyor belt from different viewing angles. By this means, they could reconstruct the light field reflected by the objects and use it to calculate all-in-focus images or depth maps. They showed, that the resulting data could successfully be employed for inspecting printed circuit boards for completeness.

In [Soukup et al., 2015], the authors use a light field camera in concert with a variable direction dome illumination in order to partially acquire the bidirectional reflectance distribution function (BRDF) of so-called diffractive optical variable image devices (OVID). OVIDs are frequently used as anti-counterfeiting measures on bank notes since their reflectance highly depends on the illumination’s angle of incidence and on the angle of observation. Because of the variable illumination direction and the angular resolution of the sample’s reflection achieved by the light field camera, the authors were able to define adequate features suitable for discriminating genuine bank notes from counterfeit ones.

In [Sudhakar et al., 2015], a special Schlieren setup is employed in concert with a compressed sensing approach to acquire light deflection maps of contact lenses. These deflection maps are similar to the deflection histograms introduced in this paper (see Sec. 5). In order to acquire the deflection maps, Sudhakar et al. illuminate the test object with parallel light beams, that are tilted with respect to the optical axis and observe the transmitted light with a telecentric camera system. Since the telecentric lens allows only light rays parallel to the optical axis to reach the sensor and since the angle of the illumination with respect to the optical axis is known, the deflection angles of the transmitted light rays can be calculated. The authors use the deflection maps to calculate the local optical power of the test object, however, they do not use it to test the inspected object for defects.

3 Light field acquisition

As shown in the previous section, there are several methods for capturing light fields. All discussed acquisition systems have different advantages and disadvantages. In order to allow the detection of even very small scattering defects in transparent materials, a potential light field sensor should have a high spatial resolution. Furthermore, there should be a convenient way of calculating the deflection angles corresponding to the captured light rays.

A common light field camera could be used together with a standard lens to capture a full light field during a single exposure [Beyerer et al., 2015]. However, for such an acquisition system, two pixels that belong to different lenslets but have the same relative position with respect to their lenslet, are sensitive for different deflection angles of the captured light rays (see Fig. 1). Therefore, further calibration steps would be needed, what would complicate further processing steps.

To overcome this drawback, this article introduces a novel optical design (see Fig. 2). The sensing part of the setup consists of a lenslet array placed in front of the sensor and of two main lenses. The optical setup can be described as a $4f$ system since the two lenses share a common focal plane and since the distance

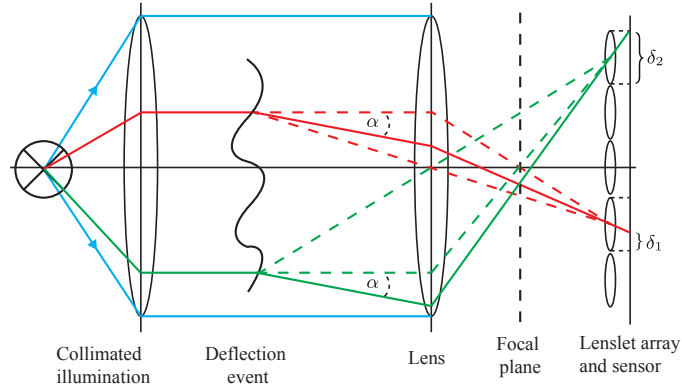


Figure 1: Spatial dependence of angular deflection measurements using a conventional light field camera: two light rays, red and green, get deflected at different spatial positions in the measurement field. Although they have the same deflection angle α , the relative pixel positions δ_1 and δ_2 , with respect to the corresponding lenslet, are different.

between the measurement field and the lenslet array is four times a focal length. By this means, pixels that are located underneath different lenslets but have the same relative position with respect to the corresponding lenslet, capture light rays with different origins but with the same range of deflection angles.

In concert with an illumination consisting of parallel rays, all the pixels corresponding to one lenslet represent a local map of the angles by which light rays get deflected inside the respective spatial position of the measuring field.

This optical system has been implemented as a plugin for the physically based rendering framework Mitsuba [Jakob, 2010]. It is used to obtain test images for the experiments described in Sec. 6.

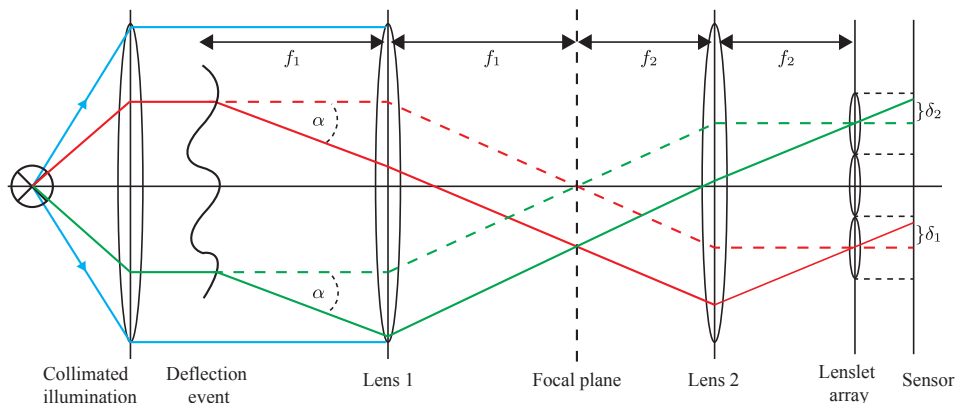


Figure 2: Measuring light deflection angles using a $4f$ system: by means of two lenses with a common focal plane, two light rays, red and green, get deflected by the same angle α at different spatial positions in the measurement field. With respect to the corresponding lenslet, the relative pixel positions δ_1 and δ_2 of the two rays are equal.

4 Mathematical framework

In the following, a framework is introduced that provides a mathematical description of light field data as it could be obtained using the optical setup described in Sec. 3. The light field processing methods presented in the next section are based on this framework.

A light field $L(x, y, \theta, \phi)$ is a function that maps a light ray starting from the position $\mathbf{p} = (x, y)^T$ with a polar angle θ and an azimuthal angle ϕ with respect to a fixed plane in 3D-space to a radiance L . In the acquisition setup from Fig. 2, the lenslet array is responsible for the spatial component, i.e., the (x, y) part of L and the sensor pixels behind each lenslet correspond to the angular information, i.e., the (θ, ϕ) part of L . Therefore, the four-dimensional light field captured using the presented sensor is represented in a 2D-image by spatially multiplexing the spatial and angular component. For demultiplexing and obtaining a more convenient access to the light field data, an alternative formulation is introduced. At first, the discretized pendants m, n, i, j, a of the continuous quantities x, y, θ, ϕ, L are defined by the mappings

$$x \mapsto m, \quad (1)$$

$$y \mapsto n, \quad (2)$$

$$\theta \mapsto i, \quad (3)$$

$$\phi \mapsto j, \quad (4)$$

$$L(x, y, \theta, \phi) \mapsto a(m, n, i, j), \quad (5)$$

which depend on the parameters of the optical system and of the sensor. The captured light field can now be expressed via a function S with

$$S: \Omega_S \rightarrow (\Omega_A \rightarrow [0, 255]): (m, n)^T \mapsto a(m, n, \cdot, \cdot), \quad (6)$$

where Ω_S and Ω_A are the sets of the spatial, respectively, the angular sampling positions and $[0, 255]$ denotes the interval of available image values. For a given spatial position $(m, n)^T$, $S(m, n) = a(m, n, \cdot, \cdot)$ is again a function providing the angular information for the respective spatial position. Figure 3 visualizes the concept of the proposed light field representation.

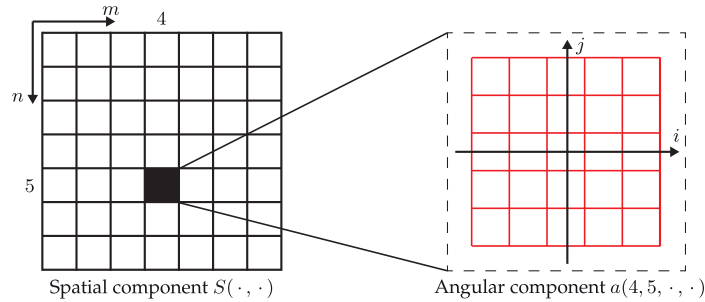


Figure 3: Proposed alternative light field representation by means of a function S , that holds the spatial component of the light field and maps a spatial position $(m, n)^T$ to a corresponding function $a(m, n, \cdot, \cdot)$ holding the respective angular light field component.

5 Light field processing

As stated before, when a defect-free transparent test object is illuminated with collimated light, the object's 3D-geometry will result in deflections of some of the incident light rays. Except for object edges or boundaries, there will be no discontinuities regarding the angular distribution of these deflections with respect to the local neighborhood. However, if the object is affected by a scattering defect (e.g., an enclosed transparent air bubble or a small absorbing particle), the respective light rays will be deflected into multiple directions and result in differences between spatially adjacent angular deflection distributions.

In order to allow a visualization or even detection of scattering defects in acquired light field data S (see Sec. 4), adequate processing steps are necessary that extract features sensitive to the mentioned discontinuities of the angular deflection distribution. For this purpose, this article proposes a chain of processing steps that will be explained in the following paragraphs.

Histogram of ray deflection (HORD) As a first preprocessing step, the input light field data S is normalized to \tilde{S} by calculating histograms out of the single angular deflection distributions:

$$\tilde{S}(m, n) := h(m, n, \cdot, \cdot), \quad (7)$$

$$h(m, n, i, j) := \frac{a(m, n, i, j)}{\sum_{(k, l) \in \Omega_A} a(m, n, k, l)}. \quad (8)$$

By this means, influences of varying light intensity are mitigated. The resulting h are called histograms of ray deflections (HORDs). Based on the HORDs, features can be calculated that allow a visualization of material defects resulting in ray deflections. The extraction of two possible features is described in the following sections.

5.1 Discontinuity extraction by histogram comparison

One possible way to find discontinuities between adjacent HORDs is to calculate a special kind of gradient

$$\tilde{\Delta}_{\tilde{S}}(m, n) = \begin{pmatrix} d(\tilde{S}(m-1, n), \tilde{S}(m+1, n)) \\ d(\tilde{S}(m, n-1), \tilde{S}(m, n+1)) \end{pmatrix} \quad (9)$$

of \tilde{S} in horizontal and vertical direction and to search for peaks in the gradient's norm $\|\tilde{\Delta}_{\tilde{S}}\|$. Now, an adequate distance $d(\cdot, \cdot)$ for two-dimensional histograms has to be defined. Since the histograms corresponding to two rays that have been deflected into different directions should result in a high difference, $d(\cdot, \cdot)$ should consider cross-bin distances.

A distance that is suitable for comparing HORDs in the demanded way is the so-called earth mover's distance $EMD(\cdot, \cdot)$, [Rubner et al., 1998]. The EMD can be imagined as the minimum costs needed for rearranging the probability mass of h_1 to form h_2 (or vice versa). The earth mover's distance is defined by:

$$EMD(h_1, h_2) := \min_{\gamma(k, l) \in \mathcal{M}} \sum_{k=1}^N \sum_{l=1}^N \gamma(k, l) c(k, l), \quad (10)$$

$$\mathcal{M} = \{\gamma(k, l) : \gamma(k, l) \geq 0, \sum_l \gamma(k, l) = h_1(k), \sum_k \gamma(k, l) = h_2(l)\}, \quad (11)$$

with h_1 and h_2 denoting two histograms with N bins, with $c(k, l)$ denoting the costs of moving one unit probability mass from bin k to bin l and with $\gamma(k, l)$ denoting the amount of probability transferred from bin k of h_1 to bin l of h_2 . Figure 4 visualizes the calculation of the one-dimensional EMD for two example histograms.

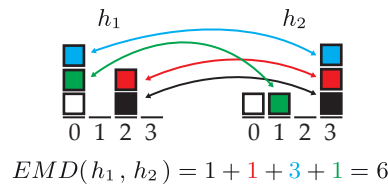


Figure 4: Example calculation of the one-dimensional earth mover's distance between the two histograms h_1 and h_2 : as visualized by the arrows, the black, red and green unit mass each have to be moved by a distance of 1 and the blue unit mass by distance of 3, resulting in an $EMD(h_1, h_2) = 6$.

Experiments carried out by using the earth mover's distance for gradient calculation on simulated images are presented in Sec. 6.

5.2 Discontinuity extraction by vector analysis

Besides histogram distances, methods of vector analysis are also suitable for extracting information on discontinuities of the local angular deflection distribution. For every HORD $\tilde{S}(m, n) = h(m, n, \cdot, \cdot)$, the mean ray

deflection direction $\bar{\mathbf{r}}(m, n)$ can be calculated as follows:

$$\bar{\mathbf{r}}(m, n) = \sum_{(i,j) \in \Omega_A} h(m, n, i, j) \cdot \mathbf{r}(i, j), \quad (12)$$

with $\mathbf{r}(i, j)$ denoting the respective deflection direction of the histogram bins (\cdot, \cdot, i, j) . The resulting vector valued function $\bar{\mathbf{r}}$ can now be considered as a vector field and can be further processed using methods of vector analysis.

As mentioned above, scattering material defects result in discontinuities of the angular deflection distribution, which is why it is sensible to look for discontinuities of $\bar{\mathbf{r}}$. Therefore, the Jacobians \mathbf{J} of $\bar{\mathbf{r}}$ can be calculated:

$$\mathbf{J}(m, n) = \begin{pmatrix} \frac{\partial \bar{r}_m}{\partial m}(m, n), & \frac{\partial \bar{r}_m}{\partial n}(m, n) \\ \frac{\partial \bar{r}_n}{\partial m}(m, n), & \frac{\partial \bar{r}_n}{\partial n}(m, n) \end{pmatrix}. \quad (13)$$

For both the m - and n -components of $\bar{\mathbf{r}}(m, n)$, the Jacobians $\mathbf{J}(m, n)$ contain the respective derivatives in m - and n -direction [Horn and Johnson, 2012]. Scattering material defects result in changes of the direction of incident rays and therefore lead to discontinuities of the angular deflection distribution. Since these discontinuities are manifested as high values of the respective components of the Jacobians \mathbf{J} , the corresponding defects can be found by applying an adequate matrix norm $\|\cdot\|$ and by looking for peaks in the resulting scalar image $\|\mathbf{J}(m, n)\|$.

Frobenius norm As mentioned above, high values of the components of $\mathbf{J}(m, n)$ might indicate that there is a defect present in the test object at position $(m, n)^T$. Hence, the Frobenius norm [Horn and Johnson, 2012] of \mathbf{J} ,

$$\|\mathbf{J}(m, n)\|_F = \sqrt{\left| \frac{\partial \bar{r}_m}{\partial m}(m, n) \right|^2 + \left| \frac{\partial \bar{r}_m}{\partial n}(m, n) \right|^2 + \left| \frac{\partial \bar{r}_n}{\partial m}(m, n) \right|^2 + \left| \frac{\partial \bar{r}_n}{\partial n}(m, n) \right|^2}, \quad (14)$$

might be a sensible choice, as it results in higher values for higher values of the single components of \mathbf{J} . However, the Frobenius norm does not take the directional information into account, that is embedded in \mathbf{J} . This characteristic of $\|\cdot\|_F$ could cause Jacobians with a high absolute value in one directional component, i.e., with a high anisotropy, to yield the same norm as Jacobians with moderate values in every directional component, i.e., with a low anisotropy.

6 Experiments

This section describes the experiments¹ conducted for evaluating the proposed light field processing approaches. Therefore, inspection images of virtual test scenes have been rendered using the physically based rendering framework Mitsuba [Jakob, 2010]. The 4f light field acquisition system introduced in Sec. 3 and shown in Fig. 2 has been implemented as a sensor plugin. Its spatial resolution has been set to 555×555 pixels and the angular resolution to 9×9 directions. The emitter plugin introduced in [Meyer et al., 2016] serves as the required parallel illumination. Furthermore, inspection images for a conventional machine vision system consisting of a telecentric camera also having a spatial resolution of 555×555 in combination with an area light source have been simulated in order to compare the proposed approach against an existing method.

A double-convex lens has been placed in the virtual scene to serve as a test object. Appropriate manipulations of the test object simulated different kinds of material defects. To all rendered inspection images, the two image processing approaches presented in Sec. 5 have been applied to evaluate their suitability for visualizing the respective types of defects. For every simulated inspection image, a gradient image using the 2D earth mover's distance and the Frobenius norm of the Jacobians of the mean deflection directions have been calculated and converted to pseudocolor images for visualization purposes. Figure 5 shows the results of the experiments.

¹All data needed for reproducing the presented results are available online at <https://www.meyer-research.de>.

For a defect-free test object, the resulting pseudocolor images have high intensities mainly at the borders of the test object. This is because the HORDs change abruptly in the respective regions. Furthermore, the sampling noise of the employed rendering framework causes single pixels to show high intensities.

In order to simulate a scattering shape defect, a part of a small sphere has been cut out of the test object in its upper left quarter by means of constructive solid geometry. Although both approaches reveal the defect, its signature seems to be stronger in the image obtained using the earth mover's distance. The conventional telecentric setup also clearly shows this defect.

In the third experiment, a small air bubble, i.e., a small scattering defect, has been placed inside the test object's center. When compared to the images corresponding to the defect-free test object, the defect is clearly visible. For this kind of defect, the earth mover's distance seems to be a particularly adequate choice, since the size of the small dot visible in the test object's center is close to the defect's actual size. In contrast to the proposed approach, the conventional inspection setup is not able to visualize the defect.

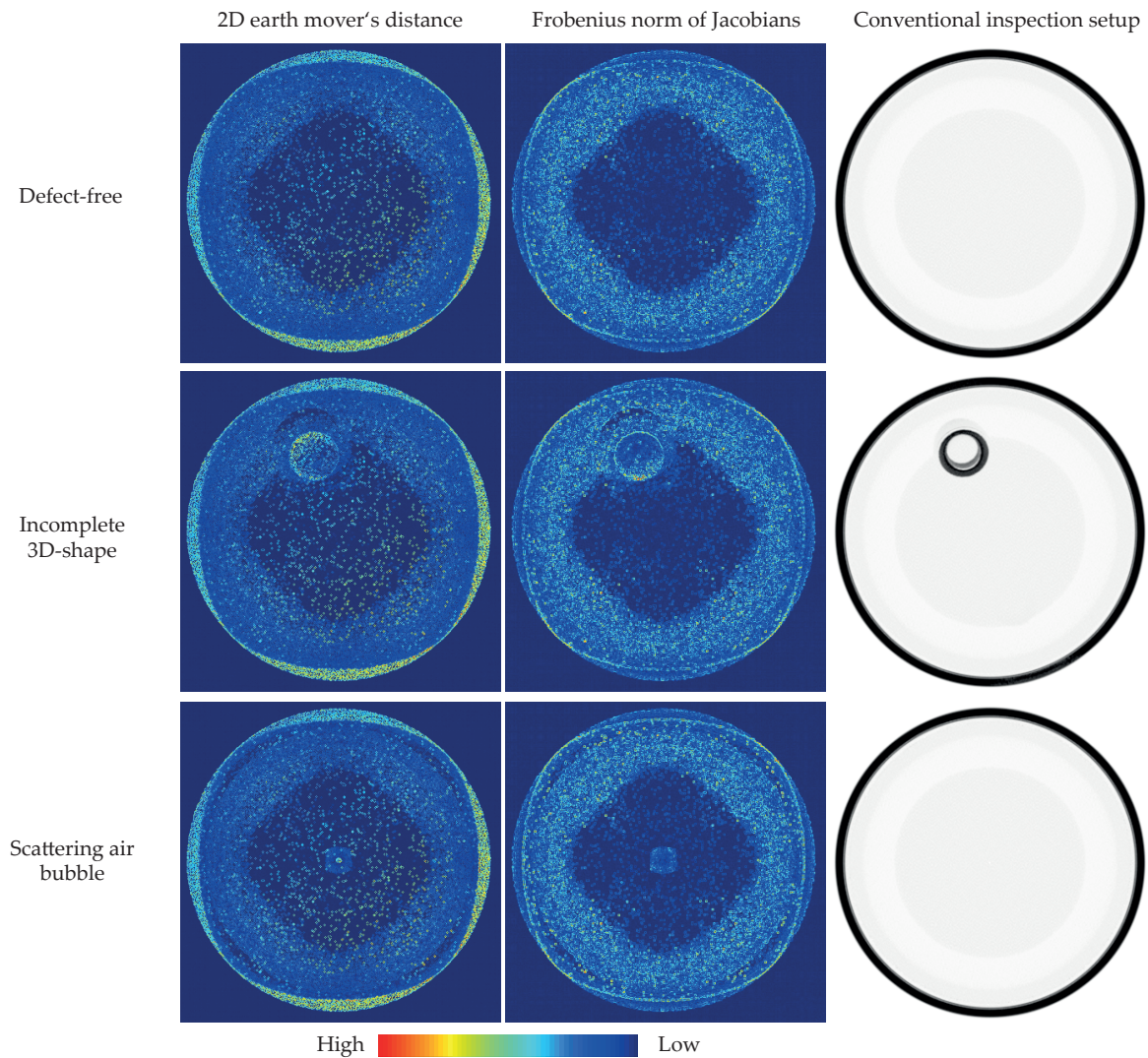


Figure 5: Results of the performed experiments.

In summary, the experiments show that the proposed image processing approaches are suitable for visualizing scattering defects in transparent materials. The earth mover's distance seems to yield images, that contain slightly more information about the defects, however, all simulated kinds of defects are also clearly visible in the images representing the Frobenius norm of the Jacobians. For small scattering inclusions, the proposed approach seems to even outperform conventional inspection methods based on telecentric camera systems.

7 Conclusion

This article introduces a $4f$ light field setup for acquiring spatially resolved histograms of ray deflections (HORDs) that can be employed for testing transparent objects for scattering material defects. Therefore, the paper presents two image processing approaches capable of visualizing these kinds of defects by extracting variations of the light's local deflection directions out of the mentioned histograms. The first approach performs histogram comparisons using the two-dimensional earth mover's distance. The second approach relies on matrix norms that are calculated for the Jacobians of the light's mean deflection direction. Simulations of the proposed acquisition setup using a physically based renderer and further processing of the resulting images show promising results stating the method's suitability for transparent object inspection.

Future work will focus on extending the proposed image processing algorithms, e.g., by supporting other histogram distances like the Bhattacharyya distance. Furthermore, a prototype of the introduced optical system will be set up in order to acquire real measurements allowing to further evaluate the approach.

References

- [Beyerer et al., 2015] Beyerer, J., León, F. P., and Frese, C. (2015). *Machine Vision: Automated Visual Inspection: Theory, Practice and Applications*. Springer Berlin Heidelberg.
- [Horn and Johnson, 2012] Horn, R. and Johnson, C. (2012). *Matrix analysis*. Cambridge University Press.
- [Jakob, 2010] Jakob, W. (2010). Mitsuba renderer. <http://www.mitsuba-renderer.org>.
- [Lippmann, 1908] Lippmann, G. (1908). Epreuves reversibles. photographies intégrales. *Comptes-Rendus de l'Académie des Sciences*, 146:446–451.
- [Meyer, 2014] Meyer, J. (2014). Visual inspection of transparent objects – physical basics, existing methods and novel ideas. Technical Report IES-2014-04, Karlsruhe Institute of Technology.
- [Meyer et al., 2016] Meyer, J., Gruna, R., Längle, T., and Beyerer, J. (2016). Simulation of an inverse schlieren image acquisition system for inspecting transparent objects. *Electronic Imaging*, 2016(19):1–9.
- [Ng et al., 2005] Ng, R., Levoy, M., Brédif, M., Duval, G., Horowitz, M., and Hanrahan, P. (2005). Light field photography with a hand-held plenoptic camera. *Computer Science Technical Report CSTR*, 2(11):1–11.
- [Perwass and Wietzke, 2012] Perwass, C. and Wietzke, L. (2012). Single lens 3d-camera with extended depth-of-field. In *IS&T/SPIE Electronic Imaging*, pages 829108–829108. International Society for Optics and Photonics.
- [Rubner et al., 1998] Rubner, Y., Tomasi, C., and Guibas, L. (1998). A metric for distributions with applications to image databases. In *Computer Vision, 1998. Sixth International Conference on*, pages 59–66. IEEE.
- [Soukup et al., 2015] Soukup, D., Štolc, S., and Huber-Mörk, R. (2015). Analysis of optically variable devices using a photometric light-field approach. In *IS&T/SPIE Electronic Imaging*, pages 94090R–94090R. International Society for Optics and Photonics.
- [Štolc et al., 2014] Štolc, S., Huber-Mörk, R., Holländer, B., and Soukup, D. (2014). Depth and all-in-focus images obtained by multi-line-scan light-field approach. In *IS&T/SPIE Electronic Imaging*, pages 902407–902407. International Society for Optics and Photonics.
- [Sudhakar et al., 2015] Sudhakar, P., Jacques, L., Dubois, X., Antoine, P., and Joannes, L. (2015). Compressive imaging and characterization of sparse light deflection maps. *SIAM Journal on Imaging Sciences*, 8(3):1824–1856.